AGU PUBLICATIONS

JGR

Journal of Geophysical Research: Atmospheres

RESEARCH ARTICLE

10.1002/2013JD021067

Key Points:

- Combining pixel and subpixel fire data improves plume height characterization
- Increasing subpixel fire area and temperature correspond to higher injections
- Filtering and clustering improve the information content of subpixel outputs

Correspondence to:
D. Peterson,
david.peterson.ctr@nrlmry.navy.mil

Citation:
Peterson, D., E. Hyer, and J. Wang (2014), Quantifying the potential for high-altitude smoke injection in the North American boreal forest using the standard MODIS fire products and subpixel-based methods, *J. Geophys. Res. Atmos.*, *119*, 3401–3419, doi:10.1002/2013JD021067.

Received 22 OCT 2013
Accepted 21 FEB 2014
Accepted article online 1 MAR 2014
Published online 27 MAR 2014

Quantifying the potential for high-altitude smoke injection in the North American boreal forest using the standard MODIS fire products and subpixel-based methods

David Peterson[1], Edward Hyer[2], and Jun Wang[3]

[1]National Research Council, Monterey, California, USA, [2]Naval Research Laboratory, Monterey, California, USA, [3]Department of Earth and Atmospheric Sciences, University of Nebraska–Lincoln, Lincoln, Nebraska, USA

Abstract All chemical transport models require an estimation of the vertical distribution of smoke particles near the source. This study quantitatively examines the strengths and weaknesses of several fire products for characterizing plume buoyancy and injection heights in the North American boreal forest during 2004–2005. Observations from the Multiangle Imaging Spectroradiometer show that 21% of smoke plumes are injected more than 500 m above the boundary layer (BL_{500}) and 8% exceed 2.5 km above ground level. Corresponding observations from the Moderate Resolution Imaging Spectroradiometer (MODIS) show that probability of injection above the BL_{500} exceeds 60% for pixel-based fire radiative power (FRP_p) values above ~2500 MW. Increasing values of subpixel-retrieved fire area and temperature also correspond to higher injections but only after removing fire pixels with a weak 11 μm fire signal and clustering. The probability of injection above the BL_{500} reaches 50% when the subpixel radiant flux (FRP_f flux) exceeds 20 kW/m^2, highlighting its potential for estimating plume buoyancy. However, these data have limitations similar to FRP_p, where the highest probability of injection corresponds to a small percentage of the data set (5–18%), and many high-altitude injections occur with lower values. Examinations of individual smoke plumes highlight the importance of combining pixel-level and subpixel outputs and show that plume injection is also sensitive to the fire pixel spatial distribution and meteorology. Therefore, an optimal method for predicting high-altitude injections will require some combination of injection climatology, FRP_p, FRP_f flux, and meteorology, but each variable's importance will depend on fire event characteristics.

1. Introduction

Global wildfire activity burns large tracts of land, releases aerosols and trace gases into the atmosphere, and produces significant impacts on life, property, air quality, weather, and even the global climate [e.g., *Randerson et al.*, 2006; *Spracklen et al.*, 2007; *Jordan et al.*, 2008; *Roy et al.*, 2008]. While the general impacts from smoke emissions are well recognized, the vertical distribution of wildfire smoke near the source is highly variable and often difficult to characterize. Many smoke plumes are confined in the boundary layer (BL), producing localized impacts on visibility and air quality. However, if a plume reaches above the BL, the atmospheric residence time increases, allowing smoke particles to be transported thousands of miles [e.g., *Westphal and Toon*, 1991; *Damoah et al.*, 2006; *Hyer et al.*, 2007; *Duck et al.*, 2007], affecting the local air quality in distant locations [e.g., *Sapkota et al.*, 2005; *Val Martin et al.*, 2013; *Dempsey*, 2013]. Smoke particles in the free troposphere have been shown to interact with meteorological processes [e.g., *Wang et al.*, 2006; *Wang et al.*, 2013] and general cloud microphysics [e.g., *Crutzen and Andreae*, 1990]. In addition, fire-generated black carbon particles can be deposited on ice sheets, which reduces the surface albedo, causing atmospheric warming and increased melting [*Randerson et al.*, 2006; *Kopacz et al.*, 2011]. Therefore, an accurate representation of the vertical profile of smoke particles, especially their maximum altitude (or injection height), is required to determine whether a given wildfire event will produce localized or widespread impacts.

Recent observationally based research has shown that 4–48% of North American smoke plumes are injected into the free troposphere, depending on plume height definition and sample size [*Kahn et al.*, 2007, 2008; *Val Martin et al.*, 2010, 2012]. This is especially true in the boreal regions, where the majority of smoke emissions are usually produced by a small fraction of the largest fire events (or blowups), which commonly occur over short time periods [*Flannigan and Harrington*, 1988; *Stocks et al*., 2002]. Regardless of location, all injection heights are driven by the initial buoyancy of the smoke plume [e.g., *Freitas et al*., 2006, 2007; *Rio et al*., 2010], which is highly dependent on fire energetics, including fire front intensity and the size of the actively burning region [e.g., *Lavoue et al*., 2000; *Val Martin et al*., 2012]. Smoke particles will only reach the free troposphere when enough buoyancy has been generated to overcome the stable region at the top of the BL. Smoke particles then become concentrated at discrete layers of increased atmospheric stability between the BL and the tropopause [*Kahn et al*., 2007; *Val Martin et al*., 2010] but may also reach into the stratosphere during rare cases of intense pyroconvection [e.g., *Fromm et al*., 2010]. In addition, the local biomass type, climate zone, and changes in meteorological conditions play an important role and typically vary from fire to fire [e.g., *Peterson et al*., 2010, 2013b]. Therefore, smoke injection heights are actually a function of geography, meteorological conditions, and fire energetics, all of which are important inputs for plume rise models.

The complex nature of the injection height problem suggests that accurate modeling of smoke transport will require detailed plume height observations for every observed fire. Unfortunately, the only two available satellite sensors that can give an indication of plume height at the global scale have severe limitations in spatial and temporal coverage. The Cloud-Aerosol Lidar with Orthogonal Polarization (CALIOP) observes only curtains over a set of north–south lines that are hundreds of kilometers apart, and sees plumes only sparingly [e.g., *Kahn et al*., 2008]. Similarly, observations from the Multiangle Imaging Spectroradiometer (MISR) can only observe a given location once every 2–8 days, and only during the daytime [e.g., *Diner et al*., 1998; *Kahn et al*., 2007, 2008]. As a result, chemical transport models currently use static assumptions about plume height. Some of the most commonly used are (1) plumes travel upward to a constant injection height based on an empirical relationship [e.g., *Lavoue et al*., 2000; *Wang et al*., 2006], (2) plumes remain well mixed in the BL [e.g., *Reid et al*., 2009], (3) plumes are uniformly mixed within the entire troposphere [e.g., *Pfister et al*., 2006], or (4) fixed fractions of plumes are released within and above the BL [e.g., *Hyer and Chew*, 2010]. By testing several of these assumptions, modeling studies have shown the potential for large biases in transport outcomes for specific fire events [e.g., *Colarco et al*., 2004]. Recent comparisons with the available CALIOP data also show that static assumptions can be systematically biased [e.g., *Wang et al*., 2013]. Moreover, static modeling approaches do not account for effects produced from the buoyancy of the fire.

As an alternative approach, several recent studies have attempted to link smoke emissions and injection heights to satellite wildfire observations, using sensors that observe global fire activity both day and night [e.g., *Jordan et al*., 2008; *Sofiev et al*., 2009, 2012; *Val Martin et al*., 2010, 2012]. For example, the Moderate Resolution Imaging Spectroradiometer (MODIS) aboard the Terra and Aqua satellites allows the thermal energy of detected fire pixels to be characterized through fire radiative power (FRP) [*Kaufman et al*., 1998]. Several recent studies have shown that FRP is proportional to the fire's fuel consumption and smoke emission rates [e.g., *Wooster*, 2002; *Wooster et al*., 2003, 2005; *Ichoku and Kaufman*, 2005; *Roberts et al*., 2005; *Ichoku et al*., 2008; *Jordan et al*., 2008]. Therefore, MODIS FRP data are currently being used for near real-time emissions maps at a global scale [*Kaiser et al*., 2012]. *Val Martin et al*. [2010] further show that fires with a high FRP and weaker atmospheric stability generally produce higher-altitude smoke plumes and a greater chance of smoke transport into the free troposphere. However, when a MODIS FRP-based fire buoyancy configuration was implemented in a 1-D plume rise model, it failed to reproduce the smoke plume heights observed by MISR and had difficulty predicting which plumes were injected above the BL [*Val Martin et al*., 2012]. MODIS FRP data are also underestimated in the presence of thick smoke or cloud cover and are influenced by the fire characteristics, including varying proportions of smoldering and flaming regions within a given fire pixel [e.g., *Kaufman et al*., 1998; *Kahn et al*., 2007].

A major drawback for interpreting current MODIS FRP data (hereafter FRP_p) in terms of fire properties is that they are estimates of fire radiative power released over a pixel area, varying from 1 km^2 at nadir to as much as 8–10 km^2 near the scan edge [e.g., *Giglio*, 2010; *Peterson et al*., 2013a]. In reality, it is the rate of energy release over the subpixel fire area that is directly related to the thermal buoyancy [*Lavoue et al*., 2000; *Kahn et al*., 2007], which directly influences the smoke injection height and the transport of smoke plumes into the free troposphere. Therefore, a calculation of fire radiative power over the subpixel area of active burning (FRP_f) could be a valuable asset to global fire monitoring [e.g., *Zhukov et al*., 2006; *Peterson et al*., 2013a] by providing estimates of the radiant energy flux over the retrieved fire area that in turn relates to the true fire intensity that drives the rise of smoke plumes [*Kahn et al*., 2007, 2008]. Recently, a subpixel retrieval of

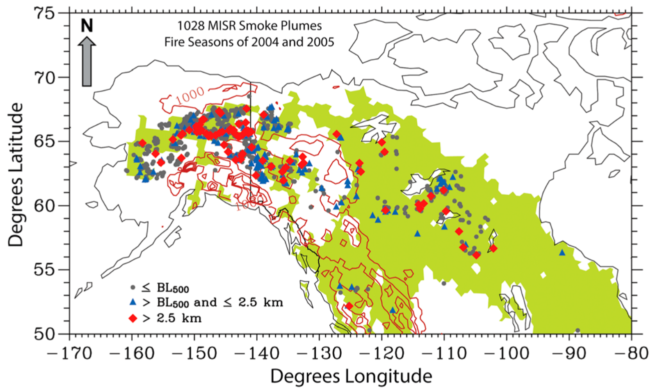

Figure 1. Map highlighting the boreal study region, extending from 80°W to 170°W longitude and from 50°N to 75°N latitude. Symbol type and color indicate the locations and smoke injection heights for the 1028 MISR smoke plumes observed during the fire seasons of 2004 and 2005. Green shading indicates the general region occupied by the boreal forest (mixed forest types), and brown contours indicate variations in topography starting at 1000 m, with a contour interval of 500 m.

instantaneous fire area and temperature has been developed specifically for MODIS fire pixels, allowing large fires burning at low intensities to be separated from smaller fires burning at high intensities [*Peterson et al*., 2013a; *Peterson and Wang*, 2013]. Subpixel information also facilitates calculations of radiant flux over the retrieved fire area.

Model simulations of smoke transport rely on meteorological inputs to drive several processes, including advection, subsidence, and diffusion. The complication with smoke plumes arises with processes that occur beneath the scale of the model grid, which may be forced by local-scale convection or driven by processes that are not included in the model simulation, such as smoke plume buoyancy, smoke self-lofting, and entrainment [*Kahn et al*., 2007; *Val Martin et al*., 2012]. Therefore, by using two years of data in the boreal forest, the goals of this investigation are to (1) incorporate MISR plume height observations to quantitatively determine which MODIS-derived fire products contain information about these subgrid-scale processes and (2) highlight the advantages and disadvantages of each variable for characterizing high-altitude injections. Subsequent sections of this paper describe the MISR smoke plume height data and the available fire products, including the additional information provided by the MODIS subpixel retrieval. Results highlight relationships between plume height observations and several fire variables, which are subsequently used to examine the general characteristics and probability of occurrence for high-altitude injection events. A detailed analysis of the meteorological component of the injection height problem will be examined in a future study.

2. Study Region, Methodology, and Data

While the fire season is fairly short, typically falling between May and September [*Skinner et al*., 1999; *Stocks et al*., 2002; *Fauria and Johnson*, 2006], the North American boreal forest is an ideal region of study due to the potential for very large, intense fire events. Previous research has also shown that boreal fire events occasionally result in large-scale smoke transport, which may reach the continental United States [e.g., *Sapkota et al*., 2005; *Duck et al*., 2007] or Europe [e.g., *Forster et al*., 2001]. The current study focuses on the core of the western boreal forest in Alaska and western Canada (Figure 1), extending from 80° to 170°W longitude and from 50° to 75°N latitude (boundaries based on *Ichoku et al*. [2008] and *Peterson et al*. [2010]). Within this region, the fire seasons of 2004 and 2005 (1 May to 30 September) were two of the three largest in the 73 year observational record [*Kasischke et al*., 2002] and provide all 1028 MISR smoke plumes used in this study. While MISR only observes a fire once in every 8 days at the equator, the coverage in the boreal regions can be as frequent as once every 2 days, thereby providing a larger quantity of available data.

2.1. MISR Smoke Plume Heights

All smoke plume height information in this study is obtained from the MISR sensor aboard the Terra satellite. MISR provides multiangle radiance imagery from a set of nine push-broom cameras, allowing the retrieval of buoyant smoke plumes and other aerosol layer heights above ground level, along with motion vectors via stereoscopic methods [*Moroney et al*., 2002; *Muller et al*., 2002]. MISR plume height data are provided at ±275 m vertical accuracy, with a horizontal resolution of 1.1 km [*Kahn et al*., 2007, 2008]. Individual smoke plumes and smoke clouds have been retrieved for several geographic regions during ~2001 and 2009 using the MISR Interactive Explorer (MINX), whereby a MINX user digitizes the source, boundaries, and smoke plume transport direction [*Nelson et al*., 2013] (http://misr.jpl.nasa.gov/getData/accessData/MisrMinxPlumes).

The output for each individual MISR data point, located within a digitized smoke plume or smoke cloud, includes smoke heights, wind speeds, albedos, and aerosol properties. A smoke plume is defined as being connected to an explicit source of Terra MODIS (MOD14) fire pixels, whereas a smoke cloud is not. Therefore, this study only incorporates smoke plume (not smoke cloud) observations with a data quality flag of "good."

The MISR plume height data are limited by potential bias and errors inherent in the digitizing process as well as the exclusion of pyroconvection events [e.g., *Val Martin et al.*, 2010]. The Aqua satellite does not have a MISR sensor; thus, only MODIS fire data obtained from the Terra satellite are applicable. In addition, the Terra daytime overpass, occurring in the late morning or early afternoon local time, does not coincide with the late afternoon maximum of observed fire intensity [e.g., *Ichoku et al.*, 2008]. MISR plume height data are also not a true tomography because thick smoke is opaque to the sensor. As a result, the height captured by the sensor is the topmost extent of smoke, less the thickness at which the accumulated extinction is sufficient to trigger detection by MISR. While additional smoke plume information is available from spaceborne lidar systems, such as CALIOP, these data are better suited for horizontally extensive, but optically thin, smoke layers located in downwind regions [e.g., *Kahn et al.*, 2008]. Therefore, despite several limitations, MISR data are the best available option for investigating smoke plume heights near the source.

The MISR plume product provides height information for every retrieved pixel in the plume, but two definitions for the entire plume boundary are also available: (1) median plume height and (2) maximum plume height. Both definitions are based on fitting a plane to all MISR observations within a given plume boundary, then removing all points more than 1.5 standard deviations from the plane. The maximum height definition is then set as the maximum height value that remains, and the median height definition is simply the median value of the remaining point heights [e.g., *Kahn et al.*, 2008; *Val Martin et al.*, 2010; *Nelson et al.*, 2013]. All MISR plume heights are provided as the height above sea level [*Kahn et al.*, 2008] and therefore must be corrected a priori for the terrain in the boreal study region (Figure 1). In this study, the maximum height definition is used because it provides an approximate upper bound on the near-source lifting associated with subgrid-scale processes. If maximum height can be successfully predicted, the problem of the distribution of smoke below the maximum height must still be solved, but it can be modeled using observations from CALIOP or other lidar systems [e.g., *Wang et al.*, 2013].

Due to the collocation of MISR and MODIS aboard the Terra satellite, this study is able to provide detailed comparisons between maximum smoke plume height and fire observations. MISR's narrow swath (360 km) [*Diner et al.*, 1998] is located in the center of the larger MODIS swath (2340 km) [*Giglio*, 2010]. Therefore, the size of each MODIS fire pixel used in this study is very close to 1 km. The MISR plume output does include limited information from the MODIS fire product, such as the total MODIS FRP_p, but a pixel-matching algorithm is required to obtain the individual MODIS fire pixels that are located within each MISR plume boundary. This study includes a buffer of 400 m around the MISR plume boundary, and all MODIS fire pixels within the buffer are assumed to be contributors to the MISR smoke plume dynamics. With many of the plumes ranging from ~20 to 80 km in length, it is possible that the smoke in downwind regions was emitted a few hours before the Terra overpass. However, this early morning period also coincides with the daily minimum in fire activity [e.g., *Ichoku et al.*, 2008]. Therefore, the fire characteristics during the late morning Terra overpass (~11 A.M. local time) are likely related to the highest observed smoke within the plume boundary.

2.2. MODIS Fire Radiative Power and the Subpixel Retrieval

The current MODIS FRP_p calculation (MOD14, collection 5) employs a best fit equation for a wide variety of fire simulations and is calculated for all fire pixels (top-of-atmosphere) using only the 4 μm channel:

$$\mathrm{FRP_p} = 4.34 \times 10^{-19}\left(T_4^8 - T_{4b}^8\right)A_\mathrm{p} \quad (1)$$

where T_{4b} is the background (or nonfire region) brightness temperature (in K), T_4 is the brightness temperature of the fire pixel, and A_p is the area of the pixel [*Kaufman et al.*, 1998; *Giglio*, 2010].

In contrast, the calculation of FRP_f is dependent on retrieved subpixel fire area and temperature, which is accomplished via a modified bispectral approach that uses lookup tables to account for the atmospheric profile (standard midlatitude summer) and variations in Earth-satellite geometry [*Peterson et al.*, 2013a; *Peterson and Wang*, 2013]. All bispectral methodologies take advantage of the spectral contrast between a pixel containing a subpixel fire hot spot and the surrounding area (assumed to be uniform) in the middle infrared (MIR, 4 μm) and thermal infrared (TIR, 11 μm) channels [e.g., *Dozier*, 1981; *Prins and Menzel*, 1992]. By assuming the 4 μm background emissivity is 0.95 [*Peterson and Wang*, 2013] and the emissivity of the fire is equal to 1 [e.g., *Giglio and Kendall*, 2001], the MODIS subpixel retrieval implements a multistep, iterative process [e.g., *Shephard and Kennelly*, 2003; *Peterson et al.*, 2013a] to identify the fire area and temperature that produce the best fit in the observed 4 and 11 μm radiances for each MODIS fire pixel in any given scene. With this information, FRP_f can be directly calculated (units of megawatts, above the mean background) via the Stefan-Boltzmann relationship in the 4 μm channel:

$$FRP_f = \sigma\left(T_f^4 - T_{4b}^4\right)A_f \tag{2}$$

where σ is the Stefan-Boltzmann constant ($5.6704 \times 10^{-8}\ \mathrm{W\,m^{-2}\,K^{-4}}$), T_f is the retrieved kinetic fire temperature at the surface (not the pixel temperature), A_f is the retrieved fire area, and T_{4b} is the 4 μm background brightness temperature, which can be used as an approximation of surface kinetic background temperature because the effects from variations in surface emissivity and atmospheric column water vapor amount are minor at low 4 μm brightness temperatures [*Peterson and Wang*, 2013]. While the FRP_f and FRP_p output is strongly correlated [*Peterson et al.*, 2013a], the subpixel information required for the FRP_f calculation provides additional information that is currently not included in the MODIS FRP_p product.

Over the past two decades, several studies have highlighted a variety of variables that may produce errors in the retrieved subpixel fire area and temperature. These include band-to-band point-spread function (PSF) coregistration issues, improper selection of background temperature and atmospheric transmittance, varying subpixel proportions and locations of flaming, smoldering, and unburned areas, and the variation of surface emissivity between the MIR and TIR [e.g., *Giglio and Kendall*, 2001; *Shephard and Kennelly*, 2003; *Giglio and Justice*, 2003]. As a result, clustering techniques are typically implemented to reduce the potential for these somewhat random errors via averaging [e.g., *Zhukov et al.*, 2006; *Wooster et al.*, 2003; *Peterson et al.*, 2013a]. For example, the individual (pixel-level) retrieved fire area and FRP_f can be summed to obtain the area and FRP_f for an entire fire event [*Peterson et al.*, 2013a], defined by the MISR plume boundaries. As an alternative approach, a single retrieval can be run on the fire pixel cluster using the mean geometry values, mean pixel temperatures, and mean background temperatures [e.g., *Zhukov et al.*, 2006; *Val Martin et al.*, 2012].

Fire pixel clustering also allows the mean FRP_f flux of each fire event to be directly calculated by

$$FRP_f\ \mathrm{Flux} = \frac{\sum_{i=1}^{n} FRP_{f_i}}{\sum_{i=1}^{n} A_{f_i}} \tag{3}$$

where the output is provided in units of $\mathrm{Wm^{-2}}$ per fire pixel cluster (using the summation method). In contrast to the FRP_p flux, which can only be calculated by using total pixel area in the denominator, the FRP_f flux calculation provides an estimation of the rate of energy release over the fire area itself. Therefore, FRP_f flux is more closely related to the thermal buoyancy of the smoke plume [*Lavoue et al.*, 2000; *Kahn et al.*, 2007]. However, when considering several potential sources of error, *Peterson and Wang* [2013] show that FRP_f flux is highly sensitive to 11 μm background temperature errors. This limitation suggests that the accuracy of FRP_f flux will increase for larger and more intense (higher FRP_f) fire events, where the 11 μm fire signal, defined by the brightness temperature difference between the flaming/smoldering and background regions ($\Delta 11$), is very large (explained in the following section).

2.3. Constraints on the Usefulness of Subpixel-Retrieved Values

By adding an additional channel at 11 μm, the MODIS subpixel retrieval can provide additional information, in the form of fire area and temperature. However, the use of an additional channel also creates additional uncertainty in the outputs. As the first large-scale application of the MODIS subpixel algorithm, this study is able to identify and filter situations where including the 11 μm channel is not advantageous. For example, Figures 2a–2c highlight the individual fire pixels and pixel clusters with very low $\Delta 11$ values (red triangles, lowest ~20% of data). The weak 11 μm fire signal produces nonphysical results, in the form of very high retrieved fire temperatures and small retrieved fire areas, which correspond to some of the lowest FRP_f values (Figure 2, contours) and affect the accuracy of the FRP_f flux calculation. There are also individual fire pixels

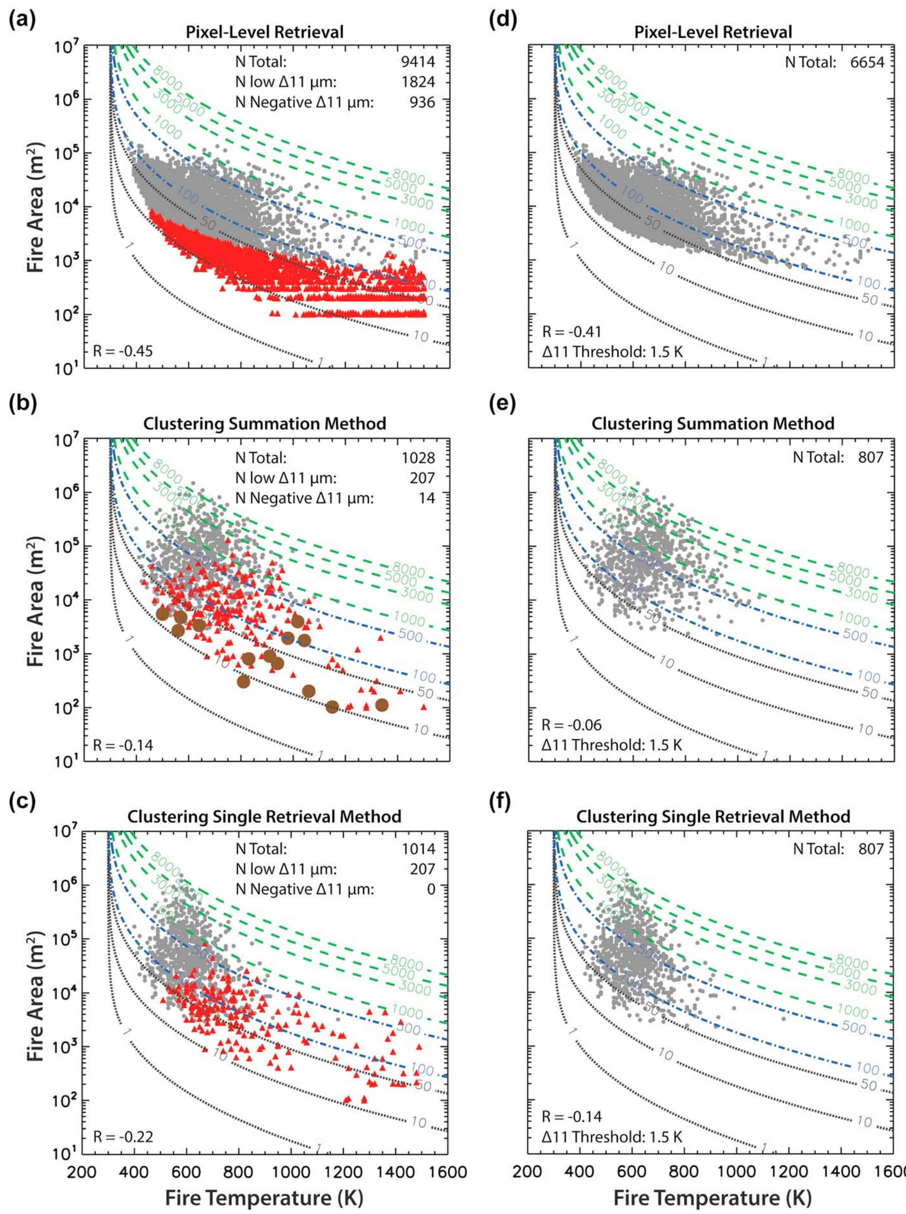

Figure 2. Subpixel fire area and temperature for the (a, d) pixel-level retrieval, (b, e) clustering summation method, and (c, f) clustering single retrieval method. Red triangles in Figures 2a–2c indicate where the Δ11 is below 1.5 K, corresponding to the lowest ~20% of the observed values. Large brown circles in Figure 2b indicate where the Δ11 remains negative after clustering. All red and brown data points are excluded in Figures 2d–2f. Contours indicate FRP_f values for a background temperature of 300 K, with dotted black, dash-dotted blue, and dashed green, respectively, indicating values of 0–99 MW, 100–999 MW, and > 1000MW. While fire area is displayed using a log scale, the *R* values reflect the linear regression.

(~10% of data) where the subpixel retrieval is rendered impossible due to a MODIS background brightness temperature that is warmer than the fire pixel (negative Δ11) [*Peterson et al.*, 2013a; *Peterson and Wang*, 2013]. These cases result from the multiple detection pathways in the MODIS MOD14 fire product, where emphasis is placed on the 4 μm channel and pixels can be flagged as fire pixels even if their Δ11 is negative [*Giglio et al.*, 2003]. At the cluster level, the Δ11 remains negative for 14 fire clusters (Figure 2b, brown circles), which are therefore excluded from the single retrieval method (Figure 2c). In addition, the majority of the pixel clusters with a fire temperature greater than 900 K contain fewer than 10 fire pixels, which likely increases the uncertainty in the subpixel output in these cases. Therefore, whether at the pixel or cluster level, low Δ11 values are detrimental to the retrieved subpixel data and must be filtered from the data set.

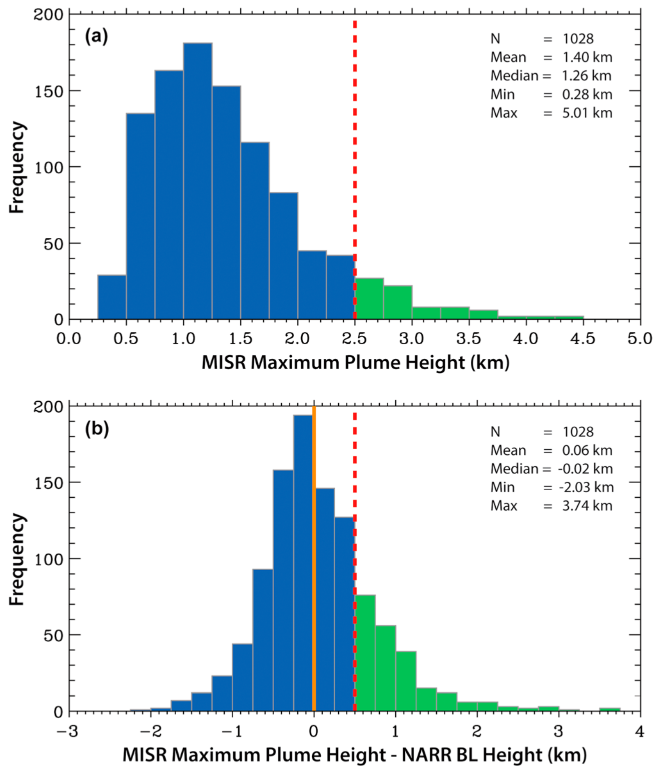

Figure 3. Histograms showing the (a) distribution of the MISR maximum plume heights and the (b) difference between maximum plume and NARR BL height using the bulk data set. Dashed red lines in Figures 3a and 3b respectively indicate the fixed 2.5 km and dynamic BL_{500} injection thresholds. Blue and green shading respectively indicate plumes with injection heights below and above each threshold, corresponding to the statistical summary in Table 1. The solid orange line in Figure 3b indicates where the plume height is equal to the NARR BL height.

Figures 2a–2c show that the lowest 20% of the observed Δ11 (red triangles) corresponds to a threshold of ~1.5 K, which forms the basis for an 11 μm filter at both the pixel and cluster levels. Any fire pixel cluster (MISR plume) with a Δ11 below 1.5 K is immediately removed from the data set, and the remaining pixel clusters are subsequently scrutinized to remove all individual pixels with a Δ11 below 1.5 K. This filtered data set (Figures 2d–2f) excludes 29% of the individual fire pixels and 21% of the pixel clusters (MISR smoke plumes), leaving 807 MISR plumes where the MODIS subpixel output is useable. The filtered data set also reduces the fraction of plumes with a mean fire temperature above 900 K from 8.4% to 1.2%. While flaming and smoldering are currently unseparated, the majority of the fire pixels/clusters dominated by smoldering will have a much weaker fire signal than the flaming dominated fires. Therefore, many of these cases will be excluded by filtering, and the remaining subpixel output will be weighted toward fire pixels/clusters with a large flaming component.

Before applying the 11 μm filter, the retrieved fire temperature and area are strongly anticorrelated at the pixel level ($R = -0.45$), and remain anticorrelated after clustering via the single retrieval ($R = -0.22$) or summation methods ($R = -0.14$). The application of the 11 μm filter causes the fire area and temperature output to become more independent, especially when using the summation clustering method ($R = -0.06$, Figure 2e). Retrieved fire area and temperature become more independent after clustering because both methodologies reduce the additional pixel-level uncertainty produced by the indirect effects described in the previous section, such as the unknown location of the individual subpixel flaming regions relative to the center of the pixel (peak in the PSF) [e.g., *Peterson et al.*, 2013a]. Therefore, both the 11 μm filter and pixel clustering steps are essential for any application of the MODIS subpixel retrieval. While filtering and clustering reduce the sample size, the large and intense fire events likely remain in the data set, which will be examined in greater detail in the following sections. For consistency, the majority of the analysis using the standard MODIS pixel-level data will also incorporate the 11 μm filtered data set (807 MISR plumes).

3. Distribution of High- and Low-Altitude Injections

While smoke at different vertical levels will experience different atmospheric processes, this study defines simplified thresholds of plume height where smoke is expected to be (1) clear of BL processes and (2) likely to experience differences in advection, even in coarse-resolution atmospheric simulations. As shown in Figure 3a, the 1028 available MISR smoke plumes have a mean height of 1.4 km, median of 1.3 km, and a range of 0.3–5.0 km, with only 81 (8%) of the plumes reaching an altitude greater than 2.5 km (Table 1). While few in number, these high-altitude plumes are the most likely candidates for injecting smoke into the free troposphere and producing large-scale smoke transport. Therefore, 2.5 km is used as the fixed definition of high-altitude injections in this study (Figure 3a, red dashed line).

Table 1. Plume Injection Statistics Based on Threshold, Data Set, and Region

Injection Threshold	Bulk Data Set			11 μm Filtered Data Set		
	Above	Below	Total	Above	Below	Total
All Smoke Plumes (Entire Study Region, Figure 1)						
2.5 km	81 (8%)	947 (92%)	1028	75 (9%)	732 (91%)	807
NARR BL + 500 m	221 (21%)	807 (79%)	1028	196 (24%)	611 (76%)	807
Alaska Smoke Plumes (West of −141° Latitude)						
2.5 km	49 (8%)	595 (92%)	644	47 (9%)	464 (91%)	511
NARR BL + 500 m	96 (15%)	548 (85%)	644	89 (17%)	422 (83%)	511
Canada Smoke Plumes (East of −141° Latitude)						
2.5 km	32 (8%)	352 (92%)	384	28 (9%)	268 (91%)	296
NARR BL + 500 m	125 (33%)	259 (67%)	384	107 (36%)	189 (64%)	296

In contrast, many modeling applications define high-altitude injections based on the height of the dynamic BL [e.g., *Val Martin et al*., 2010, 2012]. For comparison with earlier work, this study also incorporates BL height data provided by the North American Regional Reanalysis (NARR), which blends a variety of observational data into Eta model output containing 45 vertical layers across the North American continent with ~32 km grid spacing every 3 h [*Ebisuzaki*, 2004; *Mesinger et al*., 2006]. The NARR BL heights are calculated using the Noah Land Surface Model run by the National Centers for Environmental Prediction. While several cold season processes may affect the accuracy of these BL data, the only known issue with the relevant warm season data is a relatively small warm bias in surface temperature, likely caused by underestimated evapotranspiration, especially in forested regions [*Ek et al*., 2003].

By subtracting the NARR BL height from the MISR plume heights, Figure 3b shows that the majority of MISR smoke plumes reach an altitude that is just below the NARR BL (Figure 3b, solid orange line). This peak in the histogram is expected because the majority of smoke plumes have inadequate buoyancy to penetrate the stable layer located at the top of the BL [e.g., *Kahn et al*., 2007, 2008]. In addition, the distribution shown in Figure 3b suggests that the NARR is capable of representing the atmospheric stability profile within the study region, despite variations in local topography and a relatively coarse spatial resolution (~32 km). Following *Kahn et al*. [2008] and *Val Martin et al*. [2012], a smoke plume is assumed to have a high confidence of injection into the free troposphere when it has surpassed the NARR BL height plus an additional 500 m (BL_{500}; Figure 3b, red dashed line). The BL_{500} threshold results in 221 (21%) of the 1028 MISR smoke plumes being injected into the free troposphere (Table 1), with maximum plume heights recorded as high as 2 km above the BL (Figure 3b). Previous studies, using coarser-resolution BL data (e.g., 2° latitude × 2.5° longitude), have shown that 4–48% of smoke plumes are injected above the BL, depending on plume height definition, BL definition, and the region of study [e.g., *Kahn et al*., 2008; *Val Martin et al*., 2012]. Therefore, the percentage of high-altitude injections in this boreal sample falls within the expected range. While not displayed in Figure 3, the distributions of high-altitude injections using the 11 μm filtered data set are very similar (Table 1).

From a spatial perspective, 644 (63%) of the MISR smoke plume observations are located in the boreal forest of central Alaska (west of 141°W longitude, Table 1), which is primarily a result of the synoptic and mesoscale meteorological conditions during the fire seasons 2004 and 2005 [e.g., *Peterson et al*., 2010]. Of these plumes, 96 (15%) are injected above the BL_{500} threshold (Figure 1, blue triangles) and 49 (8%) are injected above the 2.5 km threshold (Figure 1, red diamond). When considering the remaining 384 plumes located in western Canada, 125 (33%) are injected above the BL_{500} threshold and 32 (8%) are injected above the 2.5 km threshold. The 11 μm filtered data set produces a similar spatial distribution for both thresholds (Table 1). Therefore, while the percentage of injections above 2.5 km is nearly constant across the study region, western Canada contains a slightly higher percentage of injections above the BL_{500} threshold. This may simply be a result of variations inherent in the digitizing process of the smoke plume data [e.g., *Val Martin et al*., 2010] but may also be related to the complex meteorological conditions in the lee of the Canadian Rocky Mountains [e.g., *Peterson et al*., 2010]. For the remaining results in this paper, the Alaska and Canada regions are merged into a single study region (Figure 1) because they experience similar fire characteristics during the typical boreal fire season [*Ichoku et al*., 2008]. Any potential effects from regional variations in meteorology will be examined in a future study.

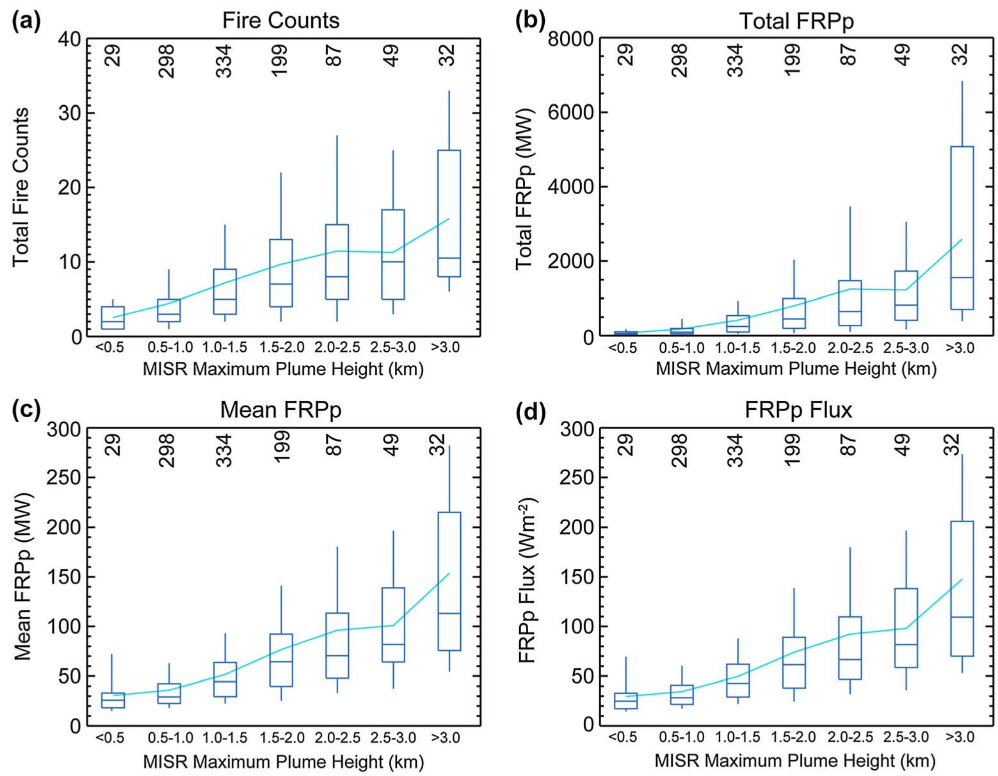

Figure 4. Distributions of the pixel-level MOD14 fire products versus MISR maximum plume height (bulk data set, $N = 1028$) using the (a) total fire counts, (b) total FRP_p, (c), mean FRP_p, and (d) FRP_p flux. The boxes are bounded by the 25th and 75th percentiles, with the median indicated as a line bisecting each box. The whiskers indicate the 10th and 90th percentiles of the data, and the mean values are displayed as a solid curve connecting each box. The corresponding number of data points is included at the top of each boxplot.

4. Signal of Plume Height in MODIS Fire Observations

As described in previous sections, the individual MODIS fire pixels within the MISR plume boundary are merged into a single pixel cluster. The single retrieval clustering method has been incorporated in several earlier studies [e.g., *Zhukov et al.*, 2005, 2006; *Val Martin et al.*, 2012] but requires a strict definition of a pixel cluster, usually based on contiguous fire pixels (or convective cores) from a single fire front. In contrast, the summation method allows the clustering criteria to be changed as needed, which is more advantageous for modeling applications covering multiple fires or multiple convective cores from the same fire front [*Peterson et al.*, 2013a]. Both clustering methodologies produce similar results for the subpixel retrieval (Figure 2). Therefore, in the following sections, the summation method is used to facilitate comparisons between MISR plume height and MODIS fire data, both at the pixel and subpixel levels.

4.1. Standard MODIS Pixel-Level Outputs

The standard MODIS fire product (MOD14) provides the number of fire pixels (or fire counts) and pixel-based FRP_p data (equation (1)) [*Giglio*, 2010], which can be examined in several ways in the context of fire pixel clusters (or smoke plume observations). By incorporating the bulk data set ($N = 1028$), Figure 4a shows that the number of MODIS fire counts increases for increasing plume heights. The 327 plumes that fail to surpass 1 km are typically associated with fewer than 5 fire pixels, while the 32 plumes above 3 km have a fire count median (mean) of 10 (15). A similar increasing relationship is observed with the total FRP_p data (Figure 4b), with lower altitude smoke plumes corresponding to FRP_p values of less than 500 MW, and higher-altitude plumes occasionally corresponding to FRP_p values greater than 3000 MW. Similar results were obtained by *Val Martin et al.* [2010] for smoke plume height data across all of North America. However, regardless of study region, considerable scatter is found within the FRP_p data, especially when

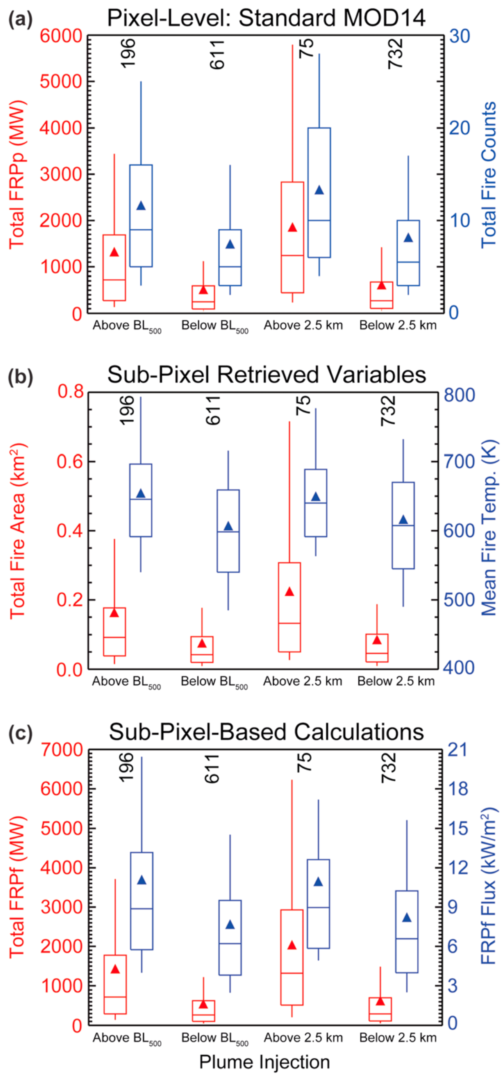

Figure 5. Distributions of the smoke plumes injected above and below the BL_{500} and 2.5 km thresholds (filtered data set, $N = 807$) based on the corresponding values (red or blue) of (a) total FRP_p and fire counts, (b) subpixel-retrieved A_{tot} and T_{mean}, and (c) total FRP_f and FRP_f flux. The boxes are bounded by the 25th and 75th percentiles, with the median indicated as a bar bisecting each box. The whiskers indicate the 10th and 90th percentiles of the data, and the mean values are displayed as red or blue triangles. The number of data points in each boxplot is included at the top of Figures 5a–5c.

the smoke plume is above 3 km (Figure 4b). As an alternative approach, the mean FRP_p can be calculated per plume (Figure 4c), which removes some of the scatter shown in Figure 4b.

When using MOD14 FRP_p data, a direct calculation of radiant heat flux is only possible when dividing by the total pixel area of the cluster (Figure 4d). In this sample, the majority of MODIS fire pixels are very close to 1 km^2 (described in section 2.1); thus, the FRP_p flux is nearly identical to the mean FRP_p. While the FRP_p flux and mean FRP_p clearly display an increasing relationship with plume height observations, these variables have limited value because their magnitude is much lower than what is expected for a typical fire event. The only alternative is to use an assumption such as the $FRP_p \times 10$ approach employed by *Val Martin et al.* [2012], which is based on fire radiative energy comprising about 10% of the total fire heat energy [e.g., *Wooster et al.*, 2005]. However, this assumption was not successful at predicting high-altitude smoke injections [*Val Martin et al.*, 2012], and therefore, FRP_p flux and mean FRP_p data provide little advantage over the total FRP_p.

Both the bulk and filtered data sets show that MODIS fire counts and FRP_p have some separability between smoke plumes that are injected above and below the BL_{500} and 2.5 km thresholds. For example, Figure 5a displays the distributions of the smoke plumes injected above and below the BL_{500} and 2.5 km thresholds (filtered data set, $N = 807$) based on the corresponding values of total FRP_p and fire counts. The distribution of FRP_p values is similar for plumes trapped below both thresholds, with a median (mean) of about 300 MW (450 MW). In contrast, the median and mean FRP_p values are about 600 MW higher for the plumes injected above 2.5 km compared to the plumes injected above the BL_{500}. The smoke plumes above 2.5 km also have much more variability in FRP_p (range > 6000 MW) compared to their counterparts located above the BL_{500} (range ~3500 MW). This results in a slightly larger separability in FRP_p for plumes above and below 2.5 km. Regardless of injection threshold, similar results are obtained for the total fire counts, confirming that high-altitude plumes are generally associated with larger and more intense fire events than the low-altitude plumes. This general relationship between plume height and the standard MODIS fire product outputs is the primary motivation for using satellite observations of fire activity to characterize smoke plume height. However, additional information is required to explore the potential value for smoke modeling applications.

In Figures 6a and 6b, the total number of injections (I_{total}), including the number of injections above (I_{above}) and below (I_{below}) the BL_{500} and 2.5 km thresholds, is stratified in terms of increasing fire counts and FRP_p. The probability of injection above the BL_{500} and 2.5 km thresholds (P_{above}) is then calculated ($P_{above} = I_{above}/I_{total}$) at each level of fire counts and FRP_p. For convenience, the corresponding I_{total} values are provided on the

10.1002/2013JD021067

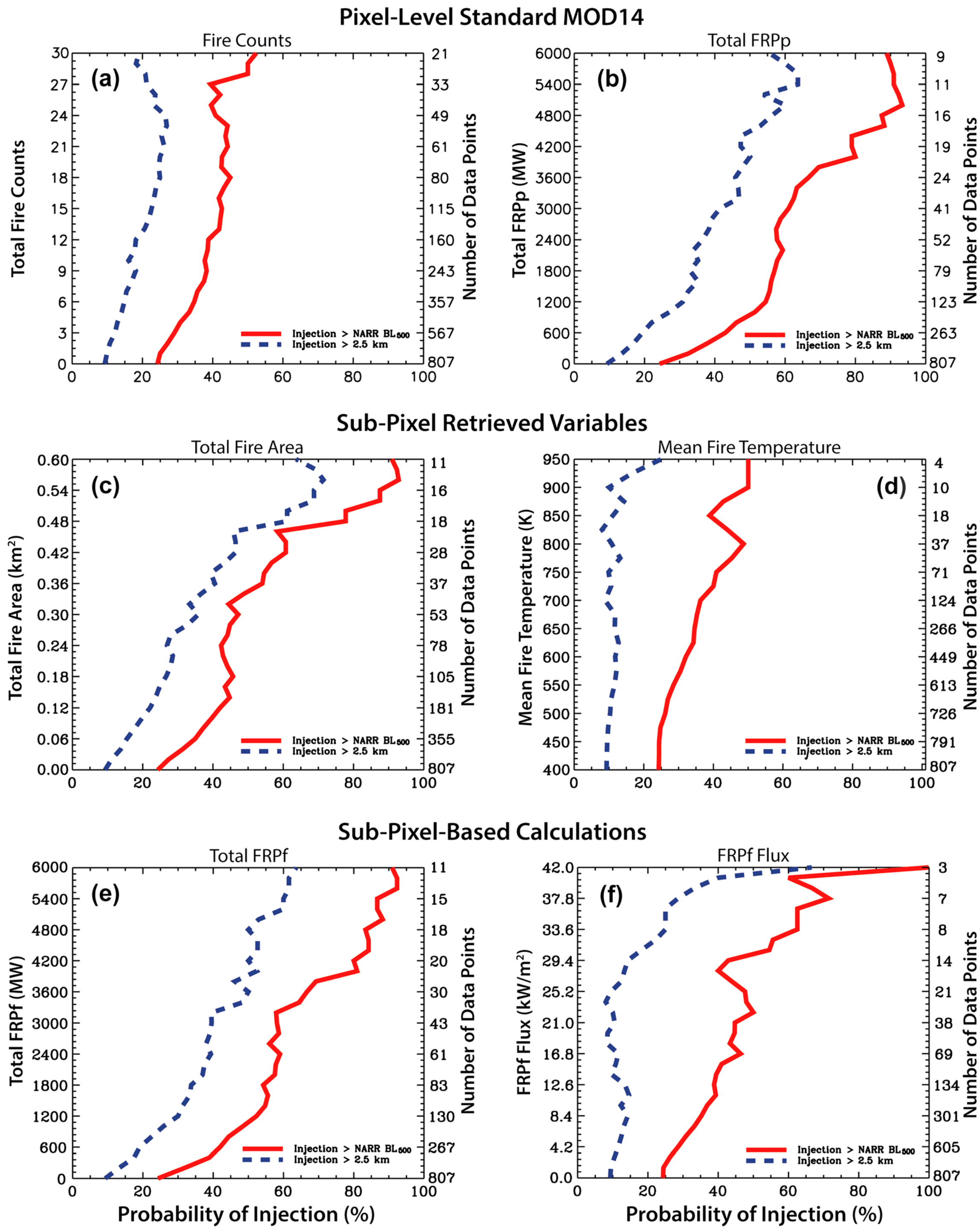

Figure 6. Probability of injection above 2.5 km (dashed blue) and the BL_{500} (solid red) as a function of (a) increasing fire counts, (b) total FRP_p, (c) A_{tot}, (d) T_{mean}, (e) total FRP_f, and (f) FRP_f flux. The corresponding number of data points is provided on the second *y* axis (based on the filtered data set, $N = 807$).

second *y* axis, allowing the variations in the both the number distribution and probability of injection to be examined in great detail. As the number of fire counts increases from 0 (no limit) to more than 30, the probability of injection above the BL_{500} (solid red) increases from 21% to 50% (Figure 6a). The probability of injection above 2.5 km (dashed blue) also increases with increasing fire counts but remains below 30%, even for the largest counts. In contrast, the probability of injection above both thresholds increases rapidly for increasing values of FRP_p (Figure 6b), and the mean FRP_p and FRP_p flux yield similar results (not shown). The probability of injection above the BL_{500} exceeds 60% for FRP_p values greater than ~2500 MW, suggesting that smoke can be placed into the free troposphere with greater confidence in these cases. However, the FRP_p probability curves also correspond to exponential decrease in the number of data points. As a result, a probability of injection above the BL_{500} of more than 60% corresponds to only ~5% of the data set.

With several high-altitude injections linked to lower FRP_p values (e.g., below 2500 MW), the standard MODIS fire product has a limited ability to characterize high-altitude injections and should only be used when the total FRP_p is greater than ~800 MW (15–20% of the data set), corresponding to at least a 50% probability of injection. All results are based solely on near-nadir fire pixels (~1 km), suggesting that injection uncertainty will increase by including fire pixels near the scan edge, which can reach sizes of 8–10 km [e.g., *Giglio*, 2010; *Peterson et al*., 2013a]. Without subpixel information, the FRP_p data are also unable to accurately represent smoke plume buoyancy. The next section examines whether retrievals of instantaneous fire size and temperature can be used to extract additional plume height signal from the MODIS fire data.

4.2. MODIS Subpixel Output

Previous studies [e.g., *Val Martin et al*., 2012] using MODIS fire data found little or no relationship between subpixel output and plume height mainly because of the complications and uncertainties that result from using the 11 μm channel in the retrieval. As a result, MODIS subpixel output has not been used in smoke modeling studies to date. However, after applying the 11 μm filter to this sample, the retrieved subpixel fire areas and temperatures show a distinct relationship with plume height (Figures 7a and 7b). In comparison to Figure 4 (bulk data set, $N = 1028$), the 11 μm filter removes several of the lower altitude injections, including 48% of the injections below 0.5 km, but the majority (> 90%) of the injections above 2.5 km remain in the data set ($N = 807$).

In the filtered data set, smoke plume heights below 1.5 km generally correspond to retrieved total fire areas (over the fire pixel cluster, A_{tot}) less than 0.15 km^2 and mean retrieved fire temperatures (T_{mean}) less than 625 K (Figures 7a and 7b). In contrast, smoke plumes injected above 2.5 km generally correspond to a retrieved T_{mean} of 600–700 K and a larger range in A_{tot}, occasionally exceeding 0.2–0.5 km^2. The retrieved T_{mean} increases with increasing plume height until ~2 km. Above this injection threshold, the median and mean of the T_{mean} remain nearly constant around 650 K. The majority of these plumes have surpassed the stable layer at the top of the BL and typically correspond to more than 8–10 fire pixels (Figure 4a), where the uncertainty in the subpixel output is reduced by averaging [e.g., *Peterson et al*., 2013a; *Peterson and Wang*, 2013]. Therefore, a large fire pixel cluster with a T_{mean} exceeding 650 K is a likely candidate for a high-altitude injection and large-scale smoke transport.

Smoke plume height comparisons using the subpixel-based FRP_f (equation (2) and Figure 7c) yield similar results to the FRP_p (equation (1) and Figure 4b), which is expected based on the output of earlier studies [e.g., *Peterson et al*., 2013a; *Peterson and Wang*, 2013]. However, the retrieved subpixel fire properties facilitate a direct calculation of fire-size based radiant flux (equation (3)), which also shows a relationship with plume height (Figure 7d). In contrast to the FRP_p flux (Figure 4d), the magnitude of the FRP_f flux is much more reasonable for the large fire events in this sample, with smoke plumes below 1.5 km generally corresponding to FRP_f flux values below 10 kW/m^2 (median of 5–7 kW/m^2) and smoke plumes above 2.5 km corresponding to a median (mean) FRP_f flux value of 9–10 kW/m^2 (10–12 kW/m^2).

In previous studies, radiant heat flux estimates were based on amount of fuel combusted, rate of fuel combustion, model simulations, or direct field measurements. *Val Martin et al*. [2012] recently employed several of these techniques and calculated mean heat flux values of 10–48 kW/m^2 for fires burning in forested regions across North America. Similarly, *Freitas et al*. [2006] compiled a literature survey for radiant flux values obtained in Brazil and found that fires in tropical forest typically fall between 30 and 80 kW/m^2, while grassland/savanna fires have a range of 3–23 kW/m^2. The FRP_f flux values in Figure 7d (boreal forest) are directly calculated from the MODIS subpixel fire data and fall at the lower end of the distribution computed by earlier studies, with a general range of 5–15 kW/m^2. Direct ground validations do not exist for this data set, but the calculated values are expected to be lower than many of the field

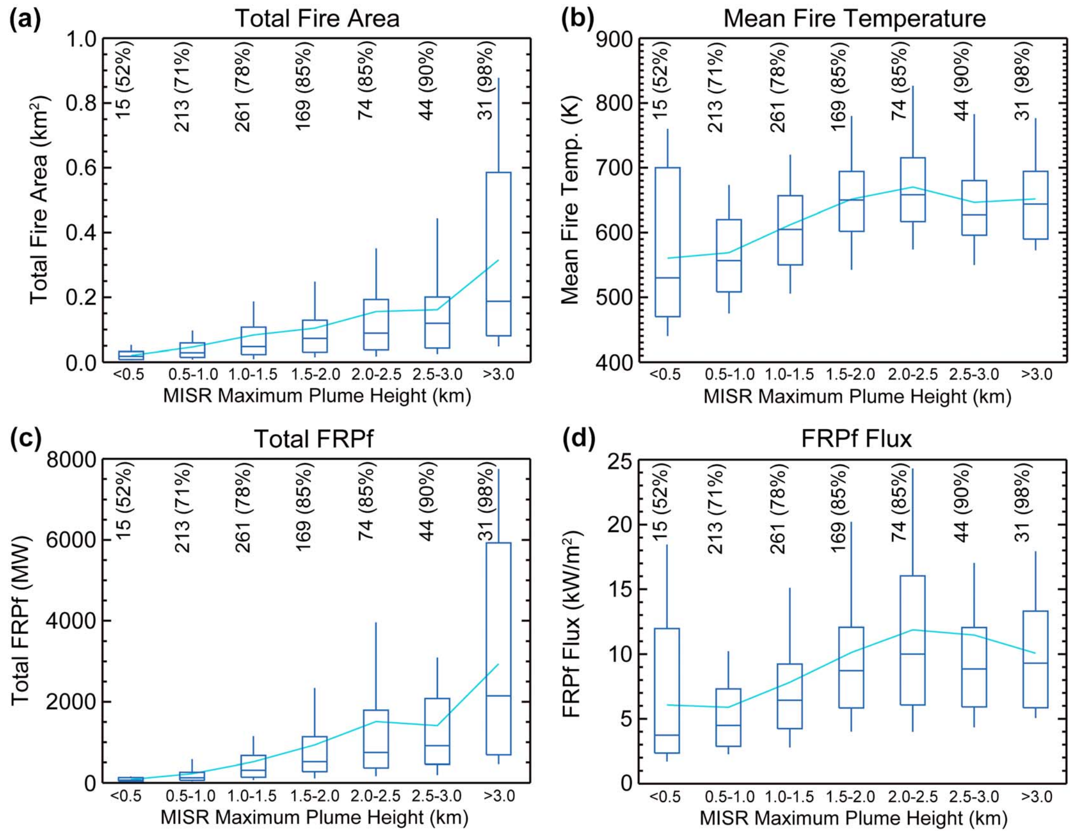

Figure 7. Distributions of the MODIS subpixel fire data versus MISR maximum plume height using the (a) A_{tot}, (b) T_{mean}, (c) total FRP_f, and (d) FRP_f flux. The boxes are bounded by the 25th and 75th percentiles, with the median indicated as a line bisecting each box. The whiskers indicate the 10th and 90th percentiles of the data, and the mean values are displayed as a solid curve connecting each box. The corresponding number of data points is included at the top of each boxplot, with the values in parentheses indicating the percentage of data remaining after applying the 11 μm filter.

measurements due to the Terra overpass occurring well before the daily maximum in observed fire activity [e.g., *Ichoku et al*., 2008]. Additionally, if the 4 μm emissivity averaged over the burning region (flaming + smoldering) is less than unity, it may contribute to the discrepancy between retrieved and measured heat flux values.

Similar to the standard MODIS fire product output (Figure 5a), the distributions of retrieved A_{tot} and T_{mean} (Figure 5b), as well as the resulting calculations of FRP_f and FRP_f flux (Figure 5c), display separability between smoke plumes that are injected above and below the BL_{500} and 2.5 km injection thresholds. While the median (and mean) T_{mean} is nearly identical for smoke plumes injected above each threshold, the median A_{tot}, and the range of retrieved A_{tot} values, is larger for plumes above the 2.5 km threshold. As shown in Figures 5b, 5c, and 7, the distributions of A_{tot} and T_{mean} are also clearly manifested in the calculations of FRP_f and FRP_f flux. The FRP_f calculation (per pixel) is highly dependent on the retrieved fire area, while the cluster's FRP_f flux is more dependent on retrieved fire temperature, which can be explained by the relative weight of each variable (A_f and T_f) in equations (2) and (3). The FRP_f flux calculation is basically an area weighting of the pixel-level T_f components in the cluster, which is especially important for mesoscale models. The majority of model grid boxes may cover several fires and therefore require some calculation of average energy over the total fire area to generate initial plume buoyancy and estimate high-altitude injection potential.

By employing the same methodology used to produce Figures 6a and 6b, the probability of injection above the 2.5 km and BL_{500} thresholds can be calculated for the subpixel outputs. Regardless of threshold, the probability of injection increases rapidly for increasing values of A_{tot} and FRP_f (Figures 6c and 6e), which is similar to the FRP_p results (Figure 6b). The probability of BL_{500} injection generally exceeds 60% when A_{tot} is greater than ~0.4 km^2 and FRP_f is greater than 2500 MW; the probability of 2.5 km injection exceeds 30–40% for those cases. While the BL_{500} injection probability increases for increasing values of T_{mean} and FRP_f flux, exceeding 40% when T_{mean} is greater than 725 K and the FRP_f flux is greater than 10 kW/m^2, the probability of 2.5 km injection is not sensitive to these retrieved values (Figures 6d and 6f). T_{mean} and FRP_f flux are the primary drivers of smoke plume buoyancy, which is critical for overcoming stable layers, such as the top of the BL. This may explain why there is a relatively large injection signal using the dynamic BL_{500} threshold in Figures 6d and 6f. In contrast, the fixed 2.5 km threshold is not dependent on atmospheric stability structure, which may explain the weak injection signal using T_{mean} and FRP_f flux.

When T_{mean} exceeds 800 K (Figure 6d), the BL_{500} probability curve becomes somewhat erratic, suggesting that the $\Delta 11$ threshold of 1.5 K may not be high enough to remove all of the erroneously high retrieved fire temperatures. This effect is not present in the A_{tot} and FRP_f results (Figures 6c and 6e) because a low $\Delta 11$ produces an erroneously small retrieved fire area. Similar to the pixel-level results, the highest probability of injection (e.g., $>$ 50%) for all subpixel outputs is limited to a small percentage of the data set (e.g., 5–18%), but many high-altitude injections occur with lower values. Therefore, while variations in viewing geometry are considered in the subpixel retrieval, FRP_f flux has limited value for characterizing high-altitude injections. The following section provides a detailed examination of selected large fire clusters, to shed light on the interaction of the different retrieved fire properties for estimating smoke plume behavior.

5. Examination of Plumes From Selected Large Fire Clusters

While the MODIS pixel and subpixel level results display some relationship to injection height in the bulk and 11 μm filtered data sets, the potential utility of these products becomes more apparent when investigating individual smoke plumes. Figure 8 and Table 2 display the results for four injection cases: (#1) low FRP_p and low injection, (#2) high FRP_p and high injection, (#3) low FRP_p and high injection, and (#4) high FRP_p and low injection. Cases #1–#4 are selected from the 73 largest fire pixel clusters, which contain at least 20 fire pixels, where the probability of injection above the BL_{500} is ~45% (Figure 6a) and random sources of error in the subpixel retrieval should be reduced by averaging [e.g., *Peterson and Wang*, 2013]. While the 11 μm filter reduces the cluster sizes by 8–35%, at least 13 fire pixels are still available for each case (Table 2).

The mean and median FRP_p values over all 73 large clusters (smoke plumes) are about 3000 MW and serve as a threshold for separating low and high FRP_p cases. The cases with both a low FRP ($<$ 3000 MW) and a low-altitude injection comprise 38% of this selection. In case #1 (Figure 8a), the total FRP_p is 954 MW and the FRP_f flux is 8.8 kW/m^2, both of which fall near the middle of the observed range for each variable and respectively correspond to an ~50% and 37% probability of injection above the BL_{500} (Figures 6b and 6f). The retrieved A_{tot} (0.1 km^2) and T_{mean} (647 K) are also fairly low (Table 2), with similar probabilities of injection above the BL_{500}. While a moderate probability of injection (40–50%) exists for this large pixel cluster, it is very close to the 45% overall probability of injection for fire pixel clusters of that size (Figure 6a). In addition, case #1 does not contain any individual pixels with a high FRP_p (e.g., $>$ 150 MW) or a high retrieved fire temperature (e.g., $>$ 800 K), and the valid pixels (after application of the $\Delta 11$ μm filter) are not concentrated around a single point. Therefore, the maximum plume height failed to surpass the height of the BL and large-scale smoke transport did not occur.

Conversely, in case #2 (Figure 8b), the total FRP_p is 5793 MW, which falls near the maximum of the observed range, and respectively corresponds to an ~60% and 90% probability of injection above the 2.5 km and BL_{500} thresholds (Figure 6b). The FRP_f flux is 11.4 kW/m^2, which falls near the middle of the observed range, and corresponds to a 40% probability of injection above the BL_{500} (Figure 6f). While the T_{mean} (643 K) is fairly modest, the retrieved A_{tot} of more than 0.5 km^2 is enormous (Table 2). Case #2 also has a highly concentrated cluster of fire pixels, with many of the individual FRP_p values exceeding 150 MW and only two pixels removed by the $\Delta 11$ μm filter. In this case, smoke was lofted to 4.84 km and transported a great distance, despite having a modest T_{mean} and FRP_f flux. Case #2 is a classic large fire event where the standard FRP_p and possibly A_{tot} information are the only predictors required for placing smoke above the BL with great confidence. These high FRP_p ($>$ 3000 MW) and high-altitude injection cases comprise 26% of the subset used in this analysis.

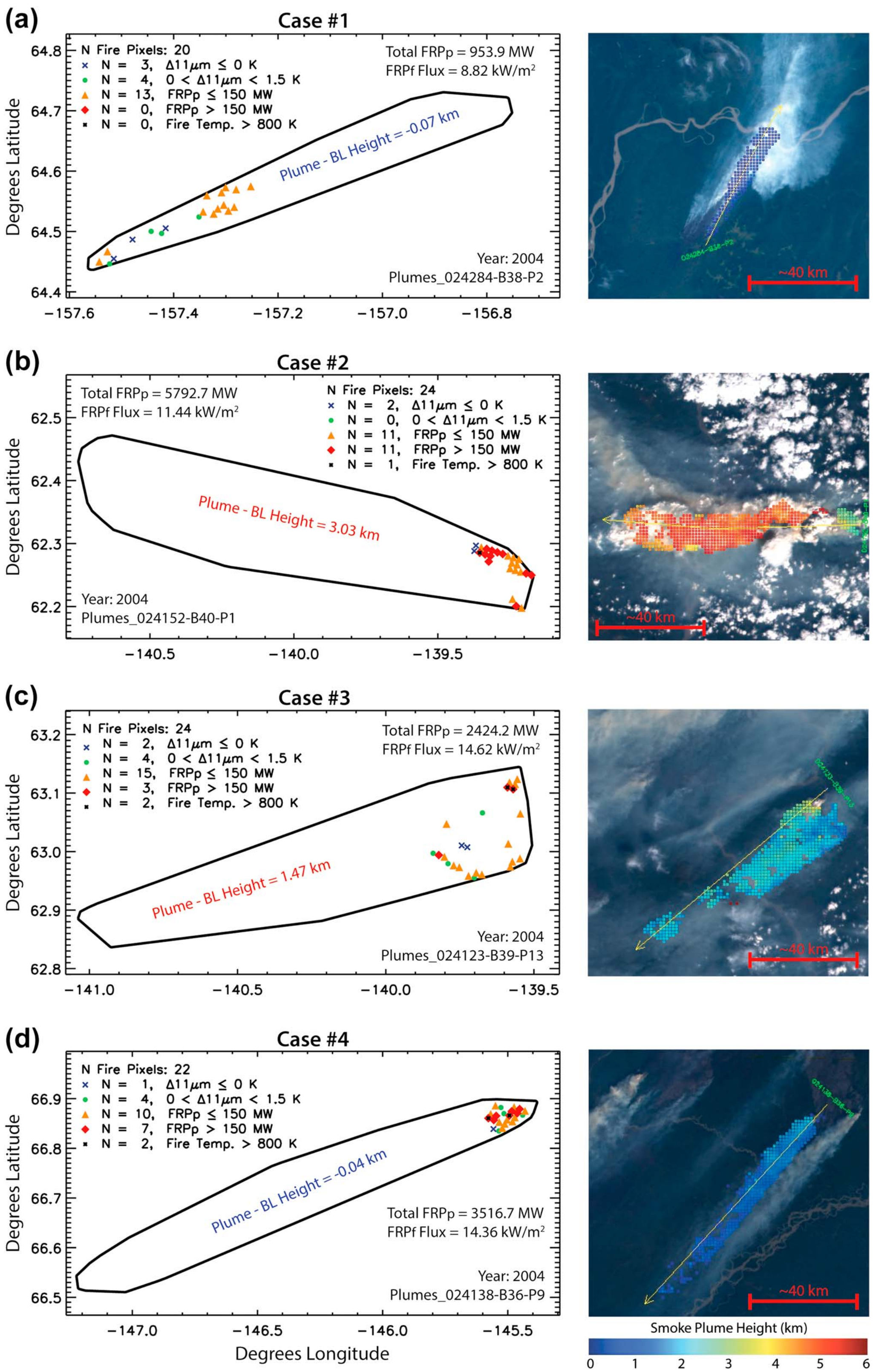

Figure 8. (left) Map and (right) corresponding MISR imagery for individual plume (a–d) cases #1–#4. Solid black contour in each map indicates the approximate smoke plume boundary derived from both the MISR digitalization process and the MISR-MODIS matching algorithm used in this study. Plot symbols and color indicate the locations and characteristics of each MODIS fire pixel within the MISR plume boundary. Shading in each MISR image indicates variations in smoke height across the plume, and yellow arrows indicate the approximate smoke transport direction. Additional details are provided in Table 2.

Table 2. Fire and Smoke Plume Characteristics for the Four Cases Displayed in Figure 8

	N Pixels All	Plume Height Max (km)	BL Height (km)	Plume-BL Height (km)	FRP_p (MW)	*N* Pixels 11 μm Filter	A_{tot} (km^2)	T_{mean} (K)	FRP_f Flux (kW/m^2)
#1, low FRP_p, low injection (Figure 8a)	20	0.88	0.95	−0.07	953.9	13	0.09	646.9	8.82
#2, high FRP_p, high injection (Figure 8b)	24	4.84	1.81	3.03	5792.7	22	0.54	642.7	11.44
#3, low FRP_p, high injection (Figure 8c)	24	2.48	1.01	1.47	2424.2	18	0.17	663.3	14.62
#4, high FRP_p, low injection (Figure 8d)	22	1.58	1.62	−0.04	3516.7	17	0.25	702.4	14.36

Several of the fire events (17%) are a hybrid of cases #1 and #2 (low FRP_p and high injection), requiring a detailed examination of both the pixel and subpixel fire data to properly estimate injection potential. For example, case #3 (Figure 8c) has a modest total FRP_p (2424 MW) for a large cluster, corresponding to a 60% and 40% probability of injection above the BL_{500} and 2.5 km thresholds (Figure 6b). With reduced confidence for a high-altitude injection using the standard pixel-level data, the subpixel output becomes critically important. In case #3, the retrieved A_{tot} is fairly small (0.17 km^2), but the T_{mean} (663 K) and FRP_f flux (14.6 kW/m^2) are higher than case #2 (Table 2). Therefore, despite a smaller fire area, case #3 has the potential to generate enough buoyancy for a high-altitude injection. From a spatial perspective, the individual fire pixels are generally less concentrated than those in case #2, and 6 (25%) of the 24 fire pixels are removed by the 11 μm filter. However, the pixels with the highest FRP_p values and retrieved fire temperatures above 800 K are concentrated in the northeast corner of the plume base. This spatial concentration, combined with elevated T_{mean} and FRP_f flux, is the key predictor indicating localized plume buoyancy sufficient to inject smoke to 2.48 km, surpassing the BL_{500} by 1.47 km, and reaching just below the fixed 2.5 km threshold.

While the subpixel data provide added value for assessing injection potential in cases #2 and #3, there are still several situations (19%) when plume behavior does not match expectations based on the fire observations. Case #4 (Figure 8d) has a large total FRP_p (3517 MW), corresponding to a 40% and 65% probability of injection above the 2.5 km and BL_{500} thresholds (Figure 6b). The retrieved A_{tot}, T_{mean}, and FRP_f flux are also very high (Table 2), and the individual fire pixels are highly concentrated, with several high FRP_p values (Figure 8d). The combination of a large total FRP_p, elevated values of all subpixel outputs, and a concentrated cluster of pixels, suggests that case #4 is a perfect candidate for a high-altitude injection. However, the plume failed to penetrate the BL. Case #4 was located in close proximity to the Fairbanks, Alaska radiosonde station (70261 PAFA, http://weather.uwyo.edu/upperair/sounding.html), which reveals that a very strong early morning inversion (~11°C at 12 Z) was present at the top of the BL and did not significantly erode by the time of the Terra overpass (21:41 Z). Therefore, even though the fire was large and intense, it could not overcome a strong stable layer. Case #4 clearly shows that MODIS pixel and subpixel-based fire data are not a complete solution for characterizing injection potential for every fire event because improved fire observations are only one component of the injection problem. As shown in several studies [e.g., *Kahn et al.*, 2007; *Val Martin et al.*, 2010], meteorological information, especially the atmospheric stability profile, must also be considered.

6. Summary and Conclusions

By incorporating MISR smoke plume height data, this study has quantitatively examined the strengths and weaknesses of several MODIS-derived fire products for characterizing smoke injection heights and initial smoke plume buoyancy in the boreal forest of North America. Emphasis is equally placed on the standard pixel-level fire products and retrieved subpixel information, including fire area, temperature, and radiant flux. Both fixed and dynamic thresholds are incorporated to identify high-altitude injections. For the region and time period of this study, 8% of the 1028 MISR smoke plumes are injected above 2.5 km and 21% are injected above the BL_{500}.

Similar to earlier studies [e.g., *Val Martin et al.*, 2010], this study has identified a general increasing relationship between the standard pixel-level MODIS fire data (near-nadir pixels) and MISR smoke plume heights. Smoke plumes injected above the 2.5 km and BL_{500} thresholds are generally associated with a larger number of fire pixels and higher FRP_p values. The probability of injection above the BL_{500} exceeds 45% for fire events with at least 20 fire pixels and 60% for FRP_p values greater than ~2500 MW, suggesting that smoke can be placed into the free troposphere with greater confidence in these cases. However, these data represent a small portion (5%) of the data set, and high-altitude injections do occur in cases where the probability of injection based on FRP_p is much lower. Standard MODIS FRP_p data also lack information on subpixel fire properties and are therefore less directly related to smoke plume buoyancy.

For the first time, this study has identified a relationship between MODIS subpixel-based fire data and smoke plume heights. However, retrieved fire area and temperature are strongly anticorrelated at the individual pixel level, meaning they are not independent. This anticorrelation can be reduced by applying a filter to remove cases with a weak 11 μm signal (low Δ11). After clustering these filtered data, the anticorrelation disappears entirely, indicating that fire size and temperature can be independently retrieved. With these steps, retrieved fire size and temperature each show a coherent relationship to plume behavior, and all subpixel outputs have different distributions for smoke plumes that are injected above and below the BL_{500} and 2.5 km injection thresholds. The probability of injection above the BL_{500} increases for increasing values of A_{tot}, T_{mean}, and FRP_f flux, but the 2.5 km probability curve responds primarily to changes in A_{tot}. While the subpixel results suggest that T_{mean} and FRP_f flux may be useful for estimating smoke plume buoyancy, these data have similar limitations to the FRP_p data, where the highest probability of injection (e.g., 50%) is limited to a small percentage of the data set (e.g., 5–18%), and many high-altitude injections occur with lower values.

An investigation of several individual smoke plumes has shown the importance of using the standard pixel-level fire data in combination with the subpixel outputs. Results clearly show that a large total FRP_p and A_{tot} (e.g., case #2) is likely to produce a high-altitude injection, even with modest values of T_{mean} and FRP_f flux. In addition, case #3 shows that subpixel information may be useful for identifying injection potential for lower FRP_p events. Results from all four individual plumes suggest that the spatial properties of the fire line within the MISR plume boundary may affect injection potential. Therefore, isolating the fire pixels that are primary contributors to the lofting of smoke may yield some improvement in satellite-based predictors of plume behavior.

The individual cases were selected because they are associated with larger numbers (>20) of fire pixels, which is necessary to reduce noise in the subpixel retrieval. However, in cases where the total FRP_p is low and the number of associated fire pixels is small, the only option is to use the climatological probability of injection for the entire data set (8% and 21% for the 2.5 km and BL_{500} thresholds). Over the next decade, the recently launched (2011) Visible Infrared Imager Radiometer Suite (VIIRS), aboard the Suomi National Polar-Orbiting Partnership mission, will gradually replace the aging MODIS sensor. VIIRS has similar fire detection capabilities at a higher spatial resolution [e.g., *Hillger et al*., 2013; *Schroederet al*., 2014; *Csiszar et al*., 2014] and therefore may improve the accuracy of satellite fire products, because of both a stronger subpixel fire signal and a larger number of available pixels to reduce noise.

While the results in this study highlight the potential utility of several fire products for improving injection height estimates, future studies must combine these satellite data with meteorological information, both within and outside the boreal forest. As shown by individual plume case #4 and several earlier studies [e.g., *Kahn et al*., 2007; *Val Martin et al*., 2010, 2012], atmospheric stability information is critically important. The effects on satellite fire observations resulting from changes in fire weather conditions must also be considered [e.g., *Peterson et al*., 2013b]. Therefore, smoke transport modeling applications will require some combination of both fire properties and weather information to estimate smoke injection heights with improved accuracy.

Acknowledgments
For this study, MISR plume height data were obtained from http://misr.jpl.nasa.gov/getData/accessData/MisrMinxPlumes and NARR boundary layer heights were obtained from http://www.esrl.noaa.gov/psd/data/gridded/data.narr.monolevel.html. The standard MODIS fire product (MOD14) can be obtained from https://lpdaac.usgs.gov/products/modis_products_table/mod14. All subpixel fire data used in this study were derived from MOD14 using the methods described in *Peterson et al*. [2013a] and may be requested via david.peterson.ctr@nrlmry.navy.mil. We thank Charles Ichoku and Ralph Kahn at the NASA Goddard Space Flight Center for their helpful advice. Early support for this project was provided by the NASA Nebraska Space grant (to Peterson). The project is currently funded at the Naval Research Laboratory in Monterey, California, by a postdoctoral fellowship award from the National Research Council (to Peterson). Hyer's contributions were supported by the NASA SEAC4RS program under NASA award NNH12AT27i. Wang acknowledges support from NASA's Applied Science Program (focus area in air quality, award NNX11AJ03G), managed by John A. Haynes, and NASA's Atmospheric Composition: Modeling and Analysis Program (award NNX13AK86G), managed by Richard S. Eckman.

References

Colarco, P. R., M. R. Schoeberl, B. G. Doddridge, L. T. Marufu, O. Torres, and E. J. Welton (2004), Transport of smoke from Canadian forest fires to the surface near Washington, D. C.: Injection height, entrainment, and optical properties, *J. Geophys. Res.*, *109*, D06203, doi:10.1029/2003JD004248.

Crutzen, P. J., and M. O. Andreae (1990), Biomass burning in the tropics—Impact on atmospheric chemistry and biogeochemical cycles, *Science*, *250*(4988), 1669–1678, doi:10.1126/science.250.4988.1669.

Csiszar, I., W. Schroeder, L. Giglio, E. Ellicott, K. P. Vadrevu, C. O. Justice, and B. Wind (2014), Active fires from the Suomi NPP Visible Infrared Imaging Radiometer Suite: Product status and first evaluation results, *J. Geophys. Res. Atmos.*, *119*, 803–816, doi:10.1002/2013JD020453.

Damoah, R., N. Spichtinger, R. Servranckx, M. Fromm, E. W. Eloranta, I. A. Razenkov, P. James, M. Shulski, C. Forster, and A. Stohl (2006), A case study of pyro-convection using transport model and remote sensing data, *Atmos. Chem. Phys.*, *6*, 173–185.

Dempsey, F. (2013), Forest fire effects on air quality in Ontario: Evaluation of several recent examples, *Bull. Am. Meteorol. Soc.*, *94*(7), 1059–1064, doi:10.1175/bams-d-11-00202.1.

Diner, D. J., et al. (1998), Multi-angle Imaging Spectroradiometer (MISR)—Instrument description and experiment overview, *IEEE Trans. Geosci. Remote Sens.*, *36*(4), 1072–1087, doi:10.1109/36.700992.

Dozier, J. (1981), A method for satellite identification of surface temperature fields of subpixel resolution, *Remote Sens. Environ.*, *11*, 221–229.

Duck, T. J., et al. (2007), Transport of forest fire emissions from Alaska and the Yukon Territory to Nova Scotia during summer 2004, *J. Geophys. Res.*, *112*, D10S44, doi:10.1029/2006JD007716.

Ebisuzaki, W. (2004), *National Climatic Data Center Data Documentation for NOAA Operational Model Archive and Distribution System (NOMADS) North American Regional Reanalysis*, edited by NOAA, pp. 1–11, Camp Springs, MD.

Ek, M. B., K. E. Mitchell, Y. Lin, E. Rogers, P. Grunmann, V. Koren, G. Gayno, and J. D. Tarpley (2003), Implementation of Noah land surface model advances in the National Centers for Environmental Prediction operational mesoscale Eta model, *J. Geophys. Res.*, *108*(D22), 8851, doi:10.1029/2002JD003296.

Fauria, M. M., and E. A. Johnson (2006), Large-scale climatic patterns control large lightning fire occurrence in Canada and Alaska forest regions, *J. Geophys. Res.*, *111*, G04008, doi:10.1029/2006JG000181.

Flannigan, M. D., and J. B. Harrington (1988), A study of the relation of meteorological variables to monthly provincial area burned by wildfire in Canada (1953–80), *J. Appl. Meteorol.*, *27*(4), 441–452.

Forster, C., et al. (2001), Transport of boreal forest fire emissions from Canada to Europe, *J. Geophys. Res.*, *106*(D19), 22,887–22,906, doi:10.1029/2001JD900115.

Freitas, S. R., K. M. Longo, and M. O. Andreae (2006), Impact of including the plume rise of vegetation fires in numerical simulations of associated atmospheric pollutants, *Geophys. Res. Lett.*, *33*, L17808, doi:10.1029/2006GL026608.

Freitas, S. R., K. M. Longo, R. Chatfield, D. Latham, M. A. F. Silva Dias, M. O. Andreae, E. Prins, J. C. Santos, R. Gielow, and J. A. Carvalho Jr. (2007), Including the sub-grid scale plume rise of vegetation fires in low resolution atmospheric transport models, *Atmos. Chem. Phys.*, *7*(13), 3385–3398, doi:10.5194/acp-7-3385-2007.

Fromm, M., D. T. Lindsey, R. Servranckx, G. Yue, T. Trickl, R. Sica, P. Doucet, and S. E. Godin-Beekmann (2010), The untold story of pyrocumulonimbus, *Bull. Am. Meteorol. Soc.*, *91*(9), 1193–1209, doi:10.1175/2010bams3004.1.

Giglio, L. (2010), MODIS collection 5 active fire product user's guide version 2.4 Rep., 1–61 pp., University of Maryland, Department of Geography.

Giglio, L., and C. O. Justice (2003), Effect of wavelength selection on characterization of fire size and temperature, *IEEE Trans. Geosci. Remote Sens.*, *24*(17), 3515–3520, doi:10.1080/0143116031000117056.

Giglio, L., and J. D. Kendall (2001), Application of the Dozier retrieval to wildfire characterization—A sensitivity analysis, *Remote Sens. Environ.*, *77*(1), 34–49.

Giglio, L., J. Descloitres, C. O. Justice, and Y. J. Kaufman (2003), An enhanced contextual fire detection algorithm for MODIS, *Remote Sens. Environ.*, *87*(2-3), 273–282, doi:10.1016/s0034-4257(03)00184-6.

Hillger, D., et al. (2013), First-light imagery from Suomi NPP VIIRS, *Bull. Am. Meteorol. Soc.*, *94*(7), 1019–1029, doi:10.1175/bams-d-12-00097.1.

Hyer, E. J., and B. N. Chew (2010), Aerosol transport model evaluation of an extreme smoke episode in Southeast Asia, *Atmos. Environ.*, *44*(11), 1422–1427, doi:10.1016/j.atmosenv.2010.01.043.

Hyer, E. J., E. S. Kasischke, and D. J. Allen (2007), Effects of source temporal resolution on transport simulations of boreal fire emissions, *J. Geophys. Res.*, *112*, D01302, doi:10.1029/2006JD007234.

Ichoku, C., and Y. J. Kaufman (2005), A method to derive smoke emission rates from MODIS fire radiative energy measurements, *IEEE Trans. Geosci. Remote Sens.*, *43*(11), 2636–2649, doi:10.1109/tgrs.2005.857328.

Ichoku, C., L. Giglio, M. J. Wooster, and L. A. Remer (2008), Global characterization of biomass-burning patterns using satellite measurements of fire radiative energy, *Remote Sens. Environ.*, *112*(6), 2950–2962, doi:10.1016/j.rse.2008.02.009.

Jordan, N. S., C. Ichoku, and R. M. Hoff (2008), Estimating smoke emissions over the US Southern Great Plains using MODIS fire radiative power and aerosol observations, *Atmos. Environ.*, *42*(9), 2007–2022, doi:10.1016/j.atmosenv.2007.12.023.

Kahn, R. A., W. H. Li, C. Moroney, D. J. Diner, J. V. Martonchik, and E. Fishbein (2007), Aerosol source plume physical characteristics from space-based multiangle imaging, *J. Geophys. Res.*, *112*, D11205, doi:10.1029/2006JD007647.

Kahn, R. A., Y. Chen, D. L. Nelson, F.-Y. Leung, Q. Li, D. J. Diner, and J. A. Logan (2008), Wildfire smoke injection heights: Two perspectives from space, *Geophys. Res. Lett.*, *35*, L04809, doi:10.1029/2007GL032165.

Kaiser, J. W., et al. (2012), Biomass burning emissions estimated with a global fire assimilation system based on observed fire radiative power, *Biogeosciences*, *9*(1), 527–554, doi:10.5194/bg-9-527-2012.

Kasischke, E. S., D. Williams, and D. Barry (2002), Analysis of the patterns of large fires in the boreal forest region of Alaska, *Int. J. Wildland Fire*, *11*(2), 131–144, doi:10.1071/wf02023.

Kaufman, Y. J., C. O. Justice, L. P. Flynn, J. D. Kendall, E. M. Prins, L. Giglio, D. E. Ward, W. P. Menzel, and A. W. Setzer (1998), Potential global fire monitoring from EOS-MODIS, *J. Geophys. Res.*, *103*(D24), 32,215–32,238.

Kopacz, M., D. L. Mauzerall, J. Wang, E. M. Leibensperger, D. K. Henze, and K. Singh (2011), Origin and radiative forcing of black carbon transported to the Himalayas and Tibetan Plateau, *Atmos. Chem. Phys.*, *11*(6), 2837–2852, doi:10.5194/acp-11-2837-2011.

Lavoue, D., C. Liousse, H. Cachier, B. J. Stocks, and J. G. Goldammer (2000), Modeling of carbonaceous particles emitted by boreal and temperate wildfires at northern latitudes, *J. Geophys. Res.*, *105*(D22), 26,871–26,890.

Mesinger, F., et al. (2006), North American regional reanalysis, *Bull. Am. Meteorol. Soc.*, *87*(3), 343–360.

Moroney, C., R. Davies, and J. P. Muller (2002), Operational retrieval of cloud-top heights using MISR data, *IEEE Trans. Geosci. Remote Sens.*, *40*(7), 1532–1540, doi:10.1109/tgrs.2002.801150.

Muller, J. P., A. Mandanayake, C. Moroney, R. Davies, D. J. Diner, and S. Paradise (2002), MISR stereoscopic image matchers: Techniques and results, *IEEE Trans. Geosci. Remote Sens.*, *40*(7), 1547–1559, doi:10.1109/tgrs.2002.801160.

Nelson, D. L., M. J. Garay, R. A. Kahn, and B. A. Dunst (2013), Stereoscopic height and wind retrievals for aerosol plumes with the MISR Interactive Explorer (MINX), *Remote Sens.*, *5*, 4593–4628, doi:10.3390/rs5094593.

Peterson, D., and J. Wang (2013), A sub-pixel-based calculation of fire radiative power from MODIS observations: 2. Sensitivity analysis and potential fire weather application, *Remote Sens. Environ.*, *129*, 231–249, doi:10.1016/j.rse.2012.10.020.

Peterson, D., J. Wang, C. Ichoku, and L. A. Remer (2010), Effects of lightning and other meteorological factors on fire activity in the North American boreal forest: Implications for fire weather forecasting, *Atmos. Chem. Phys.*, *10*(14), 6873–6888, doi:10.5194/acp-10-6873-2010.

Peterson, D., E. Hyer, and J. Wang (2013a), A short-term predictor of satellite-observed fire activity in the North American boreal forest: Toward improving the prediction of smoke emissions, *Atmos. Environ.*, *71*, 304–310, doi:10.1016/j.atmosenv.2013.01.052.

Peterson, D., J. Wang, C. Ichoku, E. Hyer, and V. Ambrosia (2013b), A sub-pixel-based calculation of fire radiative power from MODIS observations: 1 Algorithm development and initial assessment, *Remote Sens. Environ.*, *129*, 262–279, doi:10.1016/j.rse.2012.10.036.

Pfister, G. G., et al. (2006), Ozone production from the 2004 North American boreal fires, *J. Geophys. Res.*, *111*, D24S07, doi:10.1029/2006JD007695.

Prins, E. M., and W. P. Menzel (1992), Geostationary satellite detection of biomass burning in South-America, *Int. J. Remote Sens.*, *13*(15), 2783–2799.

Randerson, J. T., et al. (2006), The impact of boreal forest fire on climate warming, *Science*, *314*(5802), 1130–1132, doi:10.1126/science.1132075.

Reid, J. S., et al. (2009), Global monitoring and forecasting of biomass-burning smoke: Description of and lessons from the Fire Locating and Modeling of Burning Emissions (FLAMBE) program, *Ieee J. Sel. Top. Appl. Earth Obs. Remote Sens.*, *2*(3), 144–162, doi:10.1109/jstars.2009.2027443.

Rio, C., F. Hourdin, and A. Chedin (2010), Numerical simulation of tropospheric injection of biomass burning products by pyro-thermal plumes, *Atmos. Chem. Phys.*, *10*(8), 3463–3478.

Roberts, G., M. J. Wooster, G. L. W. Perry, N. Drake, L. M. Rebelo, and F. Dipotso (2005), Retrieval of biomass combustion rates and totals from fire radiative power observations: Application to southern Africa using geostationary SEVIRI imagery, *J. Geophys. Res.*, *110*, D21111, doi:10.1029/2005JD006018.

Roy, D. P., L. Boschetti, C. O. Justice, and J. Ju (2008), The collection 5 MODIS burned area product—Global evaluation by comparison with the MODIS active fire product, *Remote Sens. Environ.*, *112*(9), 3690–3707, doi:10.1016/j.rse.2008.05.013.

Sapkota, A., J. M. Symons, J. Kleissl, L. Wang, M. B. Parlange, J. Ondov, P. N. Breysse, G. B. Diette, P. A. Eggleston, and T. J. Buckley (2005), Impact of the 2002 Canadian forest fires on particulate matter air quality in Baltimore City, *Environ. Sci. Technol.*, *39*(1), 24–32, doi:10.1021/es035311z.

Schroeder, W., P. Oliva, L. Giglio, and I. A. Csiszar (2014), The New VIIRS 375 m active fire detection data product: Algorithm description and initial assessment, *Remote Sens. Environ.*, *143*, 85–96, doi:10.1016/j.rse.2013.12.008.

Shephard, M. W., and E. J. Kennelly (2003), Effect of band-to-band coregistration on fire property retrievals, *IEEE Trans. Geosci. Remote Sens.*, *41*(11), 2648–2661, doi:10.1109/tgrs.2003.814912.

Skinner, W. R., B. J. Stocks, D. L. Martell, B. Bonsal, and A. Shabbar (1999), The association between circulation anomalies in the mid-troposphere and area burned by wildland fire in Canada, *Theor. Appl. Climatol.*, *63*(1-2), 89–105.

Sofiev, M., R. Vankevich, M. Lotjonen, M. Prank, V. Petukhov, T. Ermakova, J. Koskinen, and J. Kukkonen (2009), An operational system for the assimilation of the satellite information on wild-land fires for the needs of air quality modelling and forecasting, *Atmos. Chem. Phys.*, *9*(18), 6833–6847.

Sofiev, M., T. Ermakova, and R. Vankevich (2012), Evaluation of the smoke-injection height from wild-land fires using remote-sensing data, *Atmos. Chem. Phys.*, *12*(4), 1995–2006, doi:10.5194/acp-12-1995-2012.

Spracklen, D. V., J. A. Logan, L. J. Mickley, R. J. Park, R. Yevich, A. L. Westerling, and D. A. Jaffe (2007), Wildfires drive interannual variability of organic carbon aerosol in the western US in summer, *Geophys. Res. Lett.*, *34*, L16816, doi:10.1029/2007GL030037.

Stocks, B. J., et al. (2002), Large forest fires in Canada, 1959–1997, *J. Geophys. Res.*, *108*(D1), 8149, doi:10.1029/2001JD000484.

Val Martin, M., J. A. Logan, R. A. Kahn, F. Y. Leung, D. L. Nelson, and D. J. Diner (2010), Smoke injection heights from fires in North America: Analysis of 5 years of satellite observations, *Atmos. Chem. Phys.*, *10*(4), 1491–1510.

Val Martin, M., R. A. Kahn, J. A. Logan, R. Paugam, M. Wooster, and C. Ichoku (2012), Space-based observational constraints for 1-D fire smoke plume-rise models, *J. Geophys. Res.*, *117*, D22204, doi:10.1029/2012JD018370.

Val Martin, M., C. L. Heald, B. Ford, A. J. Prenni, and C. Wiedinmyer (2013), A decadal satellite analysis of the origins and impacts of smoke in Colorado, *Atmos. Chem. Phys.*, *13*(15), 7429–7439, doi:10.5194/acp-13-7429-2013.

Wang, J., S. A. Christopher, U. S. Nair, J. S. Reid, E. M. Prins, J. Szykman, and J. L. Hand (2006), Mesoscale modeling of Central American smoke transport to the United States: 1. "Top-down" assessment of emission strength and diurnal variation impacts, *J. Geophys. Res.*, *111*, D05S17, doi:10.1029/2005JD006416.

Wang, J., C. Ge, Z. Yang, E. J. Hyer, J. S. Reid, B.-N. Chew, M. Mahmud, Y. Zhang, and M. Zhang (2013), Mesoscale modeling of smoke transport over the Southeast Asian Maritime Continent: Interplay of sea breeze, trade wind, typhoon, and topography, *Atmos. Res.*, *122*, 486–503, doi:10.1016/j.atmosres.2012.05.009.

Westphal, D. L., and O. B. Toon (1991), Simulations of microphysical, radiative, and dynamic processes in a continental-scale forest-fire smoke plume, *J. Geophys. Res.*, *96*(D12), 22,379–22,400, doi:10.1029/91JD01956.

Wooster, M. J. (2002), Small-scale experimental testing of fire radiative energy for quantifying mass combusted in natural vegetation fires, *Geophys. Res. Lett.*, *29*(21), 2027, doi:10.1029/2002GL015487.

Wooster, M. J., B. Zhukov, and D. Oertel (2003), Fire radiative energy for quantitative study of biomass burning: Derivation from the BIRD experimental satellite and comparison to MODIS fire products, *Remote Sens. Environ.*, *86*(1), 83–107, doi:10.1016/s0034-4257(03)00070-1.

Wooster, M. J., G. Roberts, G. L. W. Perry, and Y. J. Kaufman (2005), Retrieval of biomass combustion rates and totals from fire radiative power observations: FRP derivation and calibration relationships between biomass consumption and fire radiative energy release, *J. Geophys. Res.*, *110*, D24311, doi:10.1029/2005JD006318.

Zhukov, B., K. Briess, E. Lorenz, D. Oertel, and W. Skrbek (2005), Detection and analysis of high-temperature events in the BIRD mission, *Acta Astronaut.*, *56*(1-2), 65–71, doi:10.1016/j.actaastro.2004.09.014.

Zhukov, B., E. Lorenz, D. Oertel, M. Wooster, and G. Roberts (2006), Spaceborne detection and characterization of fires during the bi-spectral infrared detection (BIRD) experimental small satellite mission (2001–2004), *Remote Sens. Environ.*, *100*(1), 29–51, doi:10.1016/j.rse.2005.09.019.

